J. Fluid Mech. (1998), *vol.* 359, *pp.* 239–264. Printed in the United Kingdom

A numerical study of breaking waves in the surf zone

By PENGZHI LIN AND PHILIP L.-F. LIU

School of Civil and Environmental Engineering
Cornell University, Ithaca, NY 14853, USA

(Received 10 May 1997 and in revised form 15 November 1997)

This paper describes the development of a numerical model for studying the evolution of a wave train, shoaling and breaking in the surf zone. The model solves the Reynolds equations for the mean (ensemble average) flow field and the k–ϵ equations for the turbulent kinetic energy, k, and the turbulence dissipation rate, ϵ. A nonlinear Reynolds stress model (Shih, Zhu & Lumley 1996) is employed to relate the Reynolds stresses and the strain rates of the mean flow. To track free-surface movements, the volume of fluid (VOF) method is employed. To ensure the accuracy of each component of the numerical model, several steps have been taken to verify numerical solutions with either analytical solutions or experimental data. For non-breaking waves, very accurate results are obtained for a solitary wave propagating over a long distance in a constant depth. Good agreement between numerical results and experimental data has also been observed for shoaling and breaking cnoidal waves on a sloping beach in terms of free-surface profiles, mean velocities, and turbulent kinetic energy. Based on the numerical results, turbulence transport mechanisms under breaking waves are discussed.

1. Introduction

Knowledge of the wave breaking mechanism on a beach is essential to nearly all coastal processes. In practice, breaking waves are powerful agents for mixing; they can dislodge and throw sediments into suspension, which will then be carried by wave-induced steady currents such as longshore currents or rip currents. The mixing characteristics due to breaking waves in the surf zone have been investigated by many researchers (Inman, Tait & Nordstrom 1971; Battjes 1975; Svendsen & Putrevu 1994). During the last two decades significant advances have been made in both theoretical and experimental studies toward the understanding of the characteristics of breaking waves. Excellent reviews on the research progress on breaking waves and the surf zone dynamics can be found in Peregrine (1983), Battjes (1988), and Svendsen & Putrevu (1996).

Laboratory measurements of velocities and turbulence intensities in periodic breaking waves have been reported by Stive (1980), Stive & Wind (1982), Nadaoka & Kondoh (1982), Hattori & Aono (1985), Mizuguchi (1986), Nadaoka, Hino & Koyano (1989), and Ting & Kirby (1994, 1995, 1996). All of these measurements were recorded by either a hot-film anemometer or a laser Doppler velocimeter (LDV). More recently the technique of particle image velocimetry (PIV) has been used to produce instantaneous velocity distributions under breaking waves (e.g. Lin & Rockwell 1994, 1995; Skyner 1996). Turbulence velocities and thus the turbulent kinetic energy distribution

can also be calculated from the PIV data (e.g. Chang & Liu 1997). Svendsen (1987) analysed the turbulent kinetic energy data obtained up to 1985 and presented the vertical profiles of the time-average turbulent kinetic energy over one wave period at different locations in the surf zone. Svendsen showed that the turbulent kinetic energy decreases with distance from wave trough; the variation of the turbulent kinetic energy in the water column is mild and the maximum turbulence intensity (the square root of twice the turbulent kinetic energy) is only 5% to 10% of the phase speed. Ting & Kirby's (1994) data reconfirmed the earlier observations. Using the phase-averaging technique, Ting & Kirby (1994) also showed that for spilling breaker the horizontal turbulence velocities vary strongly in time near the trough region but remain almost unchanged in the lower layer. For the plunging breaker, however, the horizontal turbulence velocities vary in time throughout the entire water depth, suggesting a strong penetration of the plunging jet.

The direct measurement of the velocity field near the breaking wave crest is extremely difficult because of the aerated water and the transient nature of the water surface. However, Mizuguchi (1986) reported a set of velocity measurements for a plunging breaking wave. His data showed that the magnitude of the turbulent kinetic energy in the wave crest region is about two to three times larger than those under the trough during the initial stage of wave breaking. He observed that the vertical variation of the turbulent kinetic energy under the trough is weak. His data also indicated that the turbulent velocity components in the horizontal and vertical direction are more or less of the same order of magnitude throughout the entire flow field.

Progress in developing a numerical model for wave breaking processes has been slow for obvious reasons. First, direct numerical simulation (DNS) of the turbulent flows associated with wave breaking is still not practical. Therefore, certain turbulence closure models are necessary which require adequate understanding of the physical process. Second, the difficulties in calculating the free-surface profiles during and after wave breaking are tremendous. In the aerated area the conventional assumptions that the free surface is continuous and is a material surface are no longer valid.

Most of existing numerical models for breaking waves are based on depth-integrated equations, such as the shallow-water equation, Boussinesq equation, or Serre equation. The wave breaking process is parameterized by adding a dissipation term to the depth-integrated momentum equations. While Zelt (1991) and Karambas & Koutitas (1992) used the eddy viscosity model, Brocchini, Drago & Ivoenitti (1992) and Schäffer, Madsen & Deigaard (1993) employed the more complicated 'roller' model to incorporate the velocity distribution in the aerated region. By adjusting parameters associated with the model, the results of these models all showed very reasonable agreement with the respective laboratory data for free-surface profiles. However, the accuracy of the velocity field obtained from these models has not been established. From experimental observations, it is quite clear that the vertical velocity component becomes very strong near the toe of the roller. Therefore, the depth-integrated equations are unlikely to produce accurate solutions for the velocity field. Moreover, these models lack the capability to determine spatial distributions of the turbulent kinetic energy.

Johns (1978) and Johns & Jefferson (1980) developed a breaking wave model by coupling simplified Reynolds equations for the ensemble average (from herein referred to as the mean for simplicity) velocity field and a closure equation for the turbulent kinetic energy. An additional length scale was introduced to relate the turbulent kinetic energy and its dissipation rate. In their simplified Reynolds equations, the pressure field has been assumed hydrostatic. Moreover, their governing equations

were solved numerically in a transformed plane mapping the beach and the free surface to two parallel straight lines. Consequently, their model does not allow a multi-value free-surface configuration. Their numerical results have also not been verified directly with experimental data.

Deigaard, Fredsoe & Hedegaard (1986) employed a simplified turbulent kinetic energy k-equation to estimate the turbulence transport in the surf zone. In their simplified k-equation model, all convection processes were neglected and only the vertical turbulent diffusion process was considered in addition to the turbulence production and dissipation. Svendsen (1987) found that Deigaard *et al.*'s model overestimated the depth variation of turbulent kinetic energy when compared with the available measurements (e.g. Stive & Wind 1982; Nadaoka & Kondoh 1982; Hattori & Aono 1985). This overestimation may result from the the neglect of convection processes in their model. The difficulty in determining the proper length scale of the turbulence in the surf zone may also be the reason for the disagreement between the modelling results and experimental measurements.

More recently Lemos (1992) constructed a breaking wave model with the k–ϵ turbulence closure model. The conventional eddy viscosity model, which assumes isotropic eddy viscosity, was employed. Lemos presented two sets of numerical results: one for a breaking solitary wave and the other for breaking periodic waves. His numerical solutions, which were not compared with experimental data directly, gave highly concentrated turbulence energy intensity above the wave trough region with practically no downward spreading of turbulence by convection and diffusion. This feature is inconsistent with most of laboratory experiments reported in the literature.

Based on the brief review given above, it is clear that none of the existing numerical models can describe the wave breaking process adequately. In particular, none has been verified carefully for the velocity field (both turbulent and mean). The objective of this paper is to present the development and validation of a new model describing the wave breaking processes in the surf zone.

In the following Section, the governing equations and boundary conditions used in the model are summarized briefly. The mean flow field is governed by the Reynolds equations with a nonlinear Reynolds stress model. Further turbulence closure assumptions lead to a set of transport equations for the turbulent kinetic energy, k, and the turbulence dissipation rate, ϵ.

In § 3 numerical schemes for solving the Reynolds equations and k-ϵ equations are briefly described. The volume of fluid (VOF) method, which was originally developed by Hirt & Nichols (1981), is employed to track the free surface. The details of each numerical scheme are lengthy and can be found in the literature (e.g. Chorin 1968, 1969; Kothe, Mjolsness & Torrey 1991; Liu & Lin 1997). They are not presented in this paper. However, the numerical errors introduced by the numerical scheme are discussed in this section. An example of solitary wave propagation in a constant depth is used to demonstrate the accuracy of the overall scheme for non-breaking wave simulations.

In § 4, the model is extensively tested and verified with the experimental data for a train of cnoidal waves breaking over a gentle slope (Ting & Kirby 1996). The wave breaking is of the spilling type. Comparisons are made for the free-surface profiles, the mean velocities and the turbulent kinetic energy. The agreement between the numerical results and the experimental data is reasonably good. Finally, other physical quantities obtained from the numerical model, such as the pressure field, the eddy viscosity distribution, etc. are presented. Discussions on the role of turbulent diffusion and convection in the wave breaking processes are also given.

2. Mathematical formulation

In this section the governing equations and boundary conditions for a turbulent flow field with a free surface are summarized. The details of the derivation of these equations can be found in the literature (e.g. Launder *et al.* 1972; Launder & Spalding 1972; Launder, Reece & Rodi 1975; Rodi 1980). Only key assumptions and resulting equations are given herein for completeness.

2.1. *Governing equations*

For a turbulent flow, the velocity field and the pressure field can be decomposed into two parts: the mean velocity and pressure, $\langle u_i \rangle$ and $\langle p \rangle$, and the turbulence velocity and press ure, u_i' and p'. Thus,

$$u_i = \langle u_i \rangle + u_i'; \qquad p = \langle p \rangle + p', \tag{2.1}$$

in which $i = 1, 2, 3$ for a three-dimensional flow. If the fluid is assumed to be incompressible, the mean flow field is governed by the Reynolds equations:

$$\frac{\partial \langle u_i \rangle}{\partial x_i} = 0, \tag{2.2}$$

$$\frac{\partial \langle u_i \rangle}{\partial t} + \langle u_j \rangle \frac{\partial \langle u_i \rangle}{\partial x_j} = -\frac{1}{\rho}\frac{\partial \langle p \rangle}{\partial x_i} + g_i + \frac{1}{\rho}\frac{\partial \langle \tau_{ij} \rangle}{\partial x_j} - \frac{\partial \langle u_i' u_j' \rangle}{\partial x_j}, \tag{2.3}$$

where ρ is the density of the fluid, g_i the ith component of the gravitational acceleration, and $\langle \tau_{ij} \rangle$ the viscous stress tensor of the mean flow. For a Newtonian fluid, $\langle \tau_{ij} \rangle = 2\mu \langle \sigma_{ij} \rangle$ with μ being the molecular viscosity and $\langle \sigma_{ij} \rangle = \frac{1}{2}(\partial \langle u_i \rangle / \partial x_j + \partial \langle u_j \rangle / \partial x_i)$, the rate of strain tensor of the mean flow. In the momentum equation (2.3) the influence of the turbulence fluctuations on the mean flow field is represented by the Reynolds stress tensor, $\rho \langle u_i' u_j' \rangle$.

The transport equation for the Reynolds stress tensor can be derived from the Navier–Stokes equations theoretically (e.g. Launder *et al.* 1975). Unfortunately, the resulting equation for the Reynolds stress tensor contains terms involving higher-order correlations among turbulence velocity components and turbulent pressure. Closure assumptions are necessary to relate the higher-order correlations of the turbulent flow field to the characteristics of the mean flow field. An alternative to the Reynolds stress closure model is the so-called k–ϵ model in which the Reynolds stress tensor is assumed to be related to the strain rate of the mean flow through the algebraic nonlinear Reynolds stress model (Shih, Zhu & Lumley 1996),

$$\begin{aligned}
\rho \langle u_i' u_j' \rangle = {} & \tfrac{2}{3}\rho k \delta_{ij} - C_d \rho \frac{k^2}{\epsilon}\left(\frac{\partial \langle u_i \rangle}{\partial x_j} + \frac{\partial \langle u_j \rangle}{\partial x_i}\right) \\
& - \rho \frac{k^3}{\epsilon^2}\left[C_1\left(\frac{\partial \langle u_i \rangle}{\partial x_l}\frac{\partial \langle u_l \rangle}{\partial x_j} + \frac{\partial \langle u_j \rangle}{\partial x_l}\frac{\partial \langle u_l \rangle}{\partial x_i} - \frac{2}{3}\frac{\partial \langle u_l \rangle}{\partial x_k}\frac{\partial \langle u_k \rangle}{\partial x_l}\delta_{ij}\right)\right. \\
& + C_2\left(\frac{\partial \langle u_i \rangle}{\partial x_k}\frac{\partial \langle u_j \rangle}{\partial x_k} - \frac{1}{3}\frac{\partial \langle u_l \rangle}{\partial x_k}\frac{\partial \langle u_l \rangle}{\partial x_k}\delta_{ij}\right) \\
& \left. + C_3\left(\frac{\partial \langle u_k \rangle}{\partial x_i}\frac{\partial \langle u_k \rangle}{\partial x_j} - \frac{1}{3}\frac{\partial \langle u_l \rangle}{\partial x_k}\frac{\partial \langle u_l \rangle}{\partial x_k}\delta_{ij}\right)\right],
\end{aligned} \tag{2.4}$$

in which C_d, C_1, C_2, and C_3 are empirical coefficients, δ_{ij} the Kronecker delta, and k the turbulent kinetic energy,

$$k = \tfrac{1}{2}\langle u_i' u_i' \rangle. \tag{2.5}$$

The dissipation rate of turbulent kinetic energy ϵ is defined as

$$\epsilon = \nu \left\langle \left(\frac{\partial u_i'}{\partial x_j} \right)^2 \right\rangle, \tag{2.6}$$

where $\nu = \mu/\rho$ is the molecular kinematic viscosity.

We remark here that for the conventional eddy viscosity model $C_1 = C_2 = C_3 = 0$ in (2.4) and the eddy viscosity is expressed as

$$\nu_t = C_d \frac{k^2}{\epsilon}. \tag{2.7}$$

While the conventional eddy viscosity model (2.7) limits the applications to isotropic-eddy-viscosity turbulent flow, the nonlinear Reynolds stress model (2.4) can be applied to more general turbulent flows.

The coefficients C_2 and C_3 can be determined by using the measurements for Couette-type turbulent shear flow (Champagne, Harris & Corrsin 1970). The coefficient C_1 is approximated by $C_1 = 2C_3$, following the estimation in Shih *et al.* (1996). The coefficient C_d was given by Rodi (1980). The values for these coefficients are summarized as follows:

$$C_d = 0.09, \quad C_1 = 0.0054, \quad C_2 = -0.0171, \quad C_3 = 0.0027. \tag{2.8}$$

However, using constant coefficients may lead to violations of physics under some extreme circumstances. For example, when $(k/\epsilon)(\partial\langle u_i\rangle/\partial x_i)$ (indices not summed) $\longrightarrow \infty$, the turbulence energy $\langle u_i' u_i' \rangle$ (indices not summed) in the ith direction may become negative based on equation (2.4) and constant coefficient C_d in (2.8). To satisfy the physical constraint of non-negative turbulence energy, the realizability (Shih *et al.* 1996) is enforced to make the coefficient C_d the inverse function of $(k/\epsilon)(\partial\langle u_i\rangle/\partial x_i)$. Similarly, for nonlinear terms, the coefficients are made the inverse functions of $((k/\epsilon)(\partial\langle u_i\rangle/\partial x_j))^2$ such that in any circumstance, the nonlinear contributions will remain finite. The modified coefficients used in the present model are given as follows:

$$\left.\begin{aligned} C_d &= \frac{2}{3}\left(\frac{1}{7.4 + S_{max}}\right), \quad C_1 = \frac{1}{185.2 + D_{max}^2}, \\ C_2 &= -\frac{1}{58.5 + D_{max}^2}, \quad C_3 = \frac{1}{370.4 + D_{max}^2}, \end{aligned}\right\} \tag{2.9}$$

where $S_{max} = (k/\epsilon)\ \max\left[|\partial\langle u_i\rangle/\partial x_i| \text{ (indices not summed)}\right]$ and $D_{max} = (k/\epsilon)\ \max\left[|\partial\langle u_i\rangle/\partial x_j|\right]$. It is noted that all coefficients will return to their originally proposed values as in (2.8) when S_{max} and D_{max} approach zero.

The governing equations for k and ϵ can be derived directly from the Navier–Stokes equations. The Reynolds stress tensor only appears in the k-equation as the turbulence production term, $-\langle u_i' u_j' \rangle \partial\langle u_i\rangle/\partial x_j$. Following Rodi (1980), other higher-order

correlations of turbulence fluctuations in both the k and ϵ equations are replaced by closure conditions:

$$\frac{\partial k}{\partial t} + \langle u_j \rangle \frac{\partial k}{\partial x_j} = \frac{\partial}{\partial x_j}\left[\left(\frac{\nu_t}{\sigma_k} + \nu\right)\frac{\partial k}{\partial x_j}\right] - \langle u_i' u_j' \rangle \frac{\partial \langle u_i \rangle}{\partial x_j} - \epsilon, \tag{2.10}$$

$$\frac{\partial \epsilon}{\partial t} + \langle u_j \rangle \frac{\partial \epsilon}{\partial x_j} = \frac{\partial}{\partial x_j}\left[\left(\frac{\nu_t}{\sigma_\epsilon} + \nu\right)\frac{\partial \epsilon}{\partial x_j}\right] + C_{1\epsilon}\frac{\epsilon}{k}\nu_t\left(\frac{\partial \langle u_i \rangle}{\partial x_j} + \frac{\partial \langle u_j \rangle}{\partial x_i}\right)\frac{\partial \langle u_i \rangle}{\partial x_j} - C_{2\epsilon}\frac{\epsilon^2}{k}, \tag{2.11}$$

in which σ_k, σ_ϵ, $C_{1\epsilon}$, and $C_{2\epsilon}$ are empirical coefficients. These coefficients have been determined by performing many simple experiments; the recommended values for these coefficients are (Rodi 1980)

$$C_{1\epsilon} = 1.44, \quad C_{2\epsilon} = 1.92, \quad \sigma_k = 1.0, \quad \sigma_\epsilon = 1.3. \tag{2.12}$$

The Reynolds equations, (2.2) and (2.3), and the k–ϵ transport equations, (2.10) and (2.11), with the appropriate boundary conditions have been used to predict successfully many complex turbulent flows (e.g. Rodi 1980). The empirical coefficients given in (2.12) are surprisingly universal. In the present study the same set of values for the empirical coefficients in the k–ϵ equations is used to simulate the wave breaking process.

2.2. *Boundary and initial conditions*

Appropriate boundary conditions need to be specified. For the mean flow field, the no-slip boundary condition is imposed on the solid boundary. The application of boundary conditions on the mean free surface is less certain because the mean free surface is not clearly defined for turbulent flows (Brocchini & Peregrine 1996; Liu & Lin 1997). From the ensemble-average point of view, the mean free surface for a turbulent flow is a stripe with finite thickness where the mean density varies from that of water to that of air. The thickness depends on turbulence intensity in the vicinity. Due to the difficulty in determining this thickness, we neglect the density fluctuation near the free-surface in the present model and assume that the mean free surface for turbulent flows is defined in the same way as for the laminar flow. The zero-stress condition is imposed on the mean free surface by neglecting the effect of air flow. The inflow boundary condition is case-dependent. In general, both the free-surface displacement and mean velocities are given on the inflow boundary based on either analytical solutions or measurements. The initial condition for the mean flow is treated as still water with no wave or current motion.

For the turbulence field, near the solid boundary, the log-law distribution of mean tangential velocity in the turbulent boundary layer is applied, where the values of k and ϵ can be expressed as functions of distance from the boundary and the mean tangential velocity outside of the viscous sublayer. On the free surface, the zero-gradient boundary conditions are imposed for both k and ϵ, i.e. $\partial k/\partial n = 0$ and $\partial \epsilon/\partial n = 0$, where n is the unit normal on the free surface, based on the assumption of no turbulence exchange between the water and air. More detailed information on the boundary conditions can be found in Rodi (1980) and Liu & Lin (1997).

Special attention should be paid to the specification of the initial and inflow boundary conditions for both k and ϵ. According to equation (2.11), both the production term and dissipation term for ϵ become singular when k is zero. Furthermore, the turbulence production term in equation (2.10) is proportional to products of k itself

and the model will produce no turbulence energy if there is no turbulent kinetic energy initially. Thus, it is necessary to 'seed' a small amount of k in both the initial condition and inflow boundary condition, i.e. $k = \frac{1}{2}u_t^2$ with $u_t = \delta c$, where c is the wave celerity on the inflow boundary. The choice of δ is somewhat arbitrary and in the present computations δ is chosen to be 2.5×10^{-3}. We have also conducted numerical experiments to vary δ from 2.5×10^{-6} to 2.5×10^{-3} and found that the numerical results in the surf zone are essentially independent of the choice of δ. However, near the breaking point, the choice of δ does affect the numerical results. In general, the employment of the smaller δ slightly delays the initiation of breaking processes. The value of ϵ is estimated by using the equation $\epsilon = C_d k^2/\nu_t$ with $\nu_t = \xi\nu$, where ξ is chosen to be 0.1 in the present model. Similarly, the choice of ξ has little impact on the numerical solutions in the surf zone.

3. Numerical implementation

In the numerical model, the Reynolds equations are solved by the finite difference two-step projection method (Chorin 1968, 1969). The forward time difference method is used to discretize the time derivative. The convection terms are discretized by the combination of the central difference method and upwind method. However, only the central difference method is employed to discretize the pressure gradient terms and stress gradient terms. To track free-surface locations through the wave breaking process, the volume of fluid (VOF) method is used. The method was originally developed by Hirt & Nichols (1981) and has been modified by Kothe *et al.* (1991). This portion of the present model follows closely a computer program called RIPPLE developed by Kothe *et al.* (1991). Some modifications have been made to improve the accuracy of RIPPLE. The details of these improvements are given in Liu & Lin (1997).

The k–ϵ equations are essentially the transient convection–diffusion equations with source and sink terms. Similar to the Reynolds equations, they are solved by discretizing the convection terms with the combined central difference method and upwind method. The central difference method is used for the diffusion, production, and dissipation terms. The time derivatives are discretized by using forward time difference. The detailed implementation of the numerical model is again found in Liu & Lin (1997).

The numerical solution to the Reynolds equations in the current model is first-order accurate. Numerical errors are mainly caused by the discretization of time derivative and convection terms. Additional errors caused by the VOF method are relatively subtle and so far we have not been able to develop a systematic way to accurately estimate them. On the other hand, the numerical errors caused by the discretization of the time derivative and convection terms can be found analytically. The leading numerical errors behave very similarly to the momentum diffusion by the molecular viscosity. Considering a two-dimensional problem with $\Delta x \approx \Delta y$ and $|\langle u\rangle| \approx |\langle v\rangle|$, the numerical viscosity ν_n can be roughly estimated as

$$\nu_n \approx \frac{|\langle u\rangle|\Delta x}{2}\left(\alpha - \frac{|\langle u\rangle|\Delta t}{\Delta x}\right) \approx \frac{|\langle v\rangle|\Delta y}{2}\left(\alpha - \frac{|\langle v\rangle|\Delta t}{\Delta y}\right), \tag{3.1}$$

where α is the weighting function between the central difference method and upwind method and is usually set to 0.3. The dissipation rate of the mean flow caused by the numerical viscosity is proportional to the product of the numerical viscosity ν_n and squares of the mean velocity gradients. In order to predict how much numerical

errors affect true solutions, one needs to estimate the order of magnitude of v_n and the velocity gradients. To ensure numerical stability, we require that the Courant number, which is defined as

$$Cr = \max\left[\frac{|\langle u\rangle|\Delta t}{\Delta x}, \frac{|\langle v\rangle|\Delta t}{\Delta y}\right]$$

(for all computational cells), be less than or equal to α. In most cases, we choose $Cr = \alpha = 0.3$ so that the order of magnitude of $(\alpha - |\langle v\rangle|\Delta t/\Delta y)$ or $(\alpha - |\langle u\rangle|\Delta t/\Delta x)$ in the whole computational domain is roughly $O(10^{-1})$. To simulate a typical laboratory-scale problem, the mesh size $\Delta x \approx O(10^{-2}\text{m})$ and particle velocity $|\langle u\rangle| \approx O(5.0 \times 10^{-1}\text{m s}^{-1})$. The estimated numerical viscosity is thus $v_n \approx O(2.5 \times 10^{-4}\text{m}^2\text{ s}^{-1})$, which is very small, but is about two orders of magnitude greater than the molecular viscosity of water. Therefore, the present model cannot simulate micro effects induced by the molecular diffusion.

Fortunately, for most non-breaking water wave problems, the velocity gradients are small. Therefore, the molecular and the numerical viscosity can only cause a very small amount of energy dissipation. For breaking wave problems, the mean velocity gradient can become very large during the breaking process, which could result in large numerical dissipation. However, we found that for almost all laboratory-scale breaking wave problems, the resulting eddy viscosity v_t is of the order of magnitude of $2.5 \times 10^{-3}\text{m}^2\text{ s}^{-1}$, which is at least one order of magnitude greater than the estimated numerical viscosity. Therefore, we believe that the energy dissipation induced by the turbulence overwhelms the numerical dissipation in the breaking wave simulation.

To verify the above argument for non-breaking wave problems, we examine the propagation of a solitary wave in constant water depth. The analytical solution for the free-surface profile is given as

$$\zeta(x,t) = a\,\text{sech}^2\left[\left(\frac{3a}{4d_c^3}\right)^{1/2}(x - ct)\right], \tag{3.2}$$

where a is the wave height, d_c the constant water depth, and $c = [g(d_c + a)]^{1/2}$ the wave celerity at constant water depth. The solitary wave has the height of $a = 0.1$ m and the constant water depth is $d_c = 1.0$ m. In the numerical computations, discretizations with a uniform grid system $\Delta x = 0.1$ m and $\Delta y = 0.01$ m are used. The time step Δt is automatically adjusted during the computation to satisfy the stability constraints. The Courant number Cr and the weighting coefficient α are chosen to be 0.3. In this test, the molecular viscosity and the Reynolds stresses have been set to zero such that only the Euler equations are solved with the VOF method for free-surface tracking. Therefore, any energy loss in the numerical solution is caused by numerical errors. The velocity $\langle u\rangle$ and $\langle v\rangle$ and free-surface displacement ζ are specified at the left-hand boundary based on the Boussinesq analytical solution for a solitary wave.

Figure 1(*a*) shows comparisons of the wave profiles at different time frames between the numerical results and the analytical solutions. After propagating about 100 water depths, the numerical results are still very close to the analytical solution except for a small phase shift. Figure 1(*b*) shows the numerical results of the time histories of normalized mass and energy, which includes both kinetic energy and potential energy. We find that both mass and energy are conserved during the whole computations. From $t = 12$ s to $t = 24$ s when the solitary wave is completely within the computational domain, the error in mass is less than 0.3% and the maximum error in the total energy is only 0.9%.

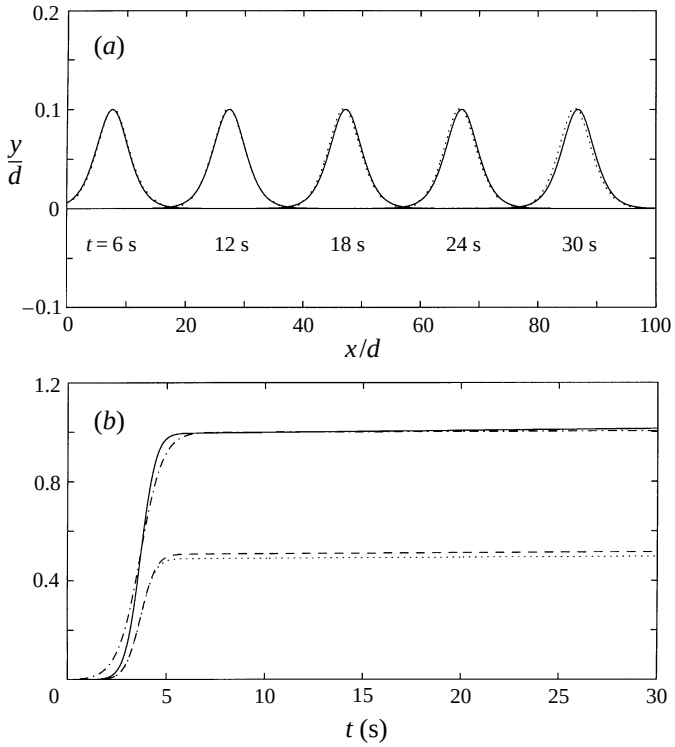

FIGURE 1. (*a*) Comparisons of solitary wave propagation in constant water depth at different time; analytical solution (—), numerical solution (· · ·). (*b*) Time histories of normalized mass (- · - ·), normalized total energy (—), kinetic energy (- - -), and potential energy (· · ·); the mass has been normalized by the calculated mass at $t = 12$ s and the energy has been normalized by the calculated total energy at $t = 12$ s.

We have also applied the numerical model to the shoaling of a non-breaking solitary wave on a beach (Liu & Lin 1997). Again, the molecular viscosity was set to zero and the k–ϵ model was not solved. The numerical results in terms of both free-surface displacement and velocities were compared to both the experimental data using PIV and accurate numerical solutions using the boundary integral equation method (BIEM). Very good agreements were obtained. All these tests for non-breaking wave problems prove the accuracy of the model which encourages us to extend it to breaking wave problems.

4. Simulation of breaking waves on a sloping beach

In this section the numerical results simulating the evolution of a cnoidal wave train breaking on a sloping beach are to be presented. Laboratory data are used to validate the numerical model first. Numerical solutions are then used to investigate some turbulent characteristics which cannot be completely revealed by the experimental data.

4.1. *Experimental setup and computational discretization*

The detailed experimental setup is given in the original papers by Ting & Kirby (1994, 1996). Only the important parameters are summarized here. The following

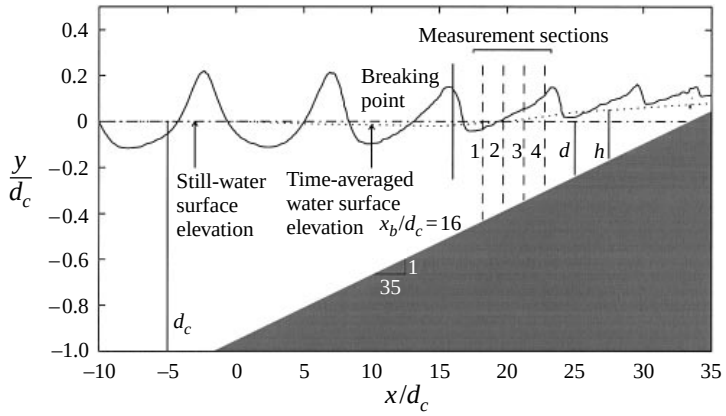

FIGURE 2. Sketch of the experimental setup and the computational domain. The still-water depth is represented by d and the time-averaged water depth is represented by $h = d + \bar{\zeta}$, where $\bar{\zeta}$ is the time-averaged water surface elevation. The beach slope is 1/35 and is connected to a constant depth $d_c = 0.4$ m. The breaking point is located at $x_b/d_c = 16.000$ and four measurement cross-sections (1–4) are located at $(x - x_b)/h_b$=4.397, 7.462, 10.528, and 13.618, where $h_b = 0.498 d_c$ is the time-averaged water depth at the breaking point.

notation is adopted in this paper: ζ is the instantaneous water surface elevation, and $\bar{\zeta} = (1/T)\int_0^T \zeta \mathrm{d}t$ is the time-average water surface elevation over one wave period T. The local still water depth is represented by d and the local time-average water depth is represented by $h = d + \bar{\zeta}$.

In the wave tank, a beach with constant slope of $s = 1/35$ is connected to a region with constant depth $d_c = 0.4$ m. The coordinate system is chosen so that $x = 0$ is located at the position where the still water depth is $d_0 = 0.38$ m (see figure 2). The incident cnoidal wave has a wave height $H = 0.125$ m in the constant-water-depth region and wave period $T = 2.0$ s. From the laboratory records, waves break at $x_b = 6.4$ m with the time-average water depth of $h_b = 0.199$ m. The velocities and free-surface displacement were measured at six vertical cross-sections shoreward of the breaking point. The mean velocities and free-surface displacement were computed by performing phase averaging of the measured data 20 minutes after the first wave was generated. The turbulence velocities were extracted from the data after the mean velocities were obtained. The data measured at $(x - x_b)/h_b = 4.397, 7.462, 10.528$, and 13.618 will be used for comparisons with the numerical results (These cross-sections are shown in figure 2 as 1, 2, 3, and 4, respectively).

In the numerical simulations, the computational domain starts at $x = -4.3$ m instead of the actual location of the wave maker to reduce the computational effort. The whole domain is discretized into a 900×77 grid system with a uniform grid in the x-direction, $\Delta x = 0.025$ m, and a non-uniform grid in the y-direction with the minimum grid $\Delta y_{min} = 0.006$ m being distributed near the free surface. The time step is automatically adjusted during the computation to satisfy the stability constraints. Both the mean velocities and free-surface displacement are specified on the left-hand boundary ($x = -4.3$ m) based on the analytical solution for cnoidal waves.

4.2. *Comparison of experimental data and numerical results*

In this section, comparisons between the experimental data and numerical results are presented for the normalized mean free-surface displacement, mean velocities, and turbulence intensity. In the experiments, the mean quantities were obtained by

performing phase averaging after the waves had reached the quasi-steady state. These phase-average quantities should be very close to the ensemble-average quantities which were obtained from the numerical model. However, the turbulence field calculated by using the phase-average method may also contains the noise generated by random waves during the breaking process. Furthermore, in the experiments, only two components of turbulence velocities were measured by LDV and the total turbulent kinetic energy was estimated by the empirical formula after Svendsen (1987), i.e. $k = \frac{2}{3}(\langle u'^2\rangle + \langle v'^2\rangle)$, where $\langle u'^2\rangle^{1/2}$ and $\langle v'^2\rangle^{1/2}$ are turbulence velocities in the horizontal and vertical direction, respectively. This approximation may also introduce some uncertainties in the following comparisons.

In our computations, in order to reduce the computational effort, we did not calculate the wave propagation for the entire experimental period, 20 minutes, which would have corresponded to the passage of 600 waves and would have required about 960 CPU hours using a single processor of supercomputer IBM SP2. Instead, numerical solutions presented herein are from $t' = 16.6$ s to $t' = 18.6$ s with $t' = 0.0$ s representing the beginning of the numerical simulation. This particular initial time $t' = 16.6$ s matches with the time $t/T = 0$ in the phase-average experimental results and it corresponds to the passage of the ninth wave past the lateral boundary in the numerical results. The computed results for mean velocities and free-surface profiles indicate that the computed waves in the surf zone have nearly, but not completely, reached the quasi-steady state, i.e. there is very small difference between two successive wave cycles. This difference suggests that the setup and setdown has not fully developed and thus the calculated mean water depth can be inaccurate. Therefore, when we make the comparisons, we must realize that the difference between the numerical results and experimental data might be partly caused by the fact that our numerical results have not reached the quasi-steady state. Nevertheless, the major wave and turbulent characteristics under breaking waves should be well captured by the numerical simulations.

Figures 3 to 6 show the comparisons at four vertical cross-sections in the surf zone. At each location, comparisons are made at four different elevations below the trough level. The figures in the left-hand column are measurements and those in the right-hand column are numerical results. Free-surface displacements are normalized by the local time-average water depth h and the mean velocities and turbulence intensities are normalized by the local phase velocity $C = (gh)^{1/2}$. It is noted that to be consistent, we use measured h in the normalization for both laboratory data and numerical results.

Figure 3 shows the comparisons at $(x - x_b)/h_b = 4.397$, which is the measurement section closest to the breaking point (see figure 2). The overall agreement between the experimental data and the numerical results for the free-surface displacement and mean velocity components is reasonable. However, numerical results overestimate the mean velocities.

The pattern of turbulence intensity in the simulation results (figure 3 *d*) is quite different from that in the measurements (figure 3 *D*). The experimental data show no obvious correlation between the turbulence intensity and the passage of the broken wave, which is quite different from the turbulence characteristics at other measurement sections in the surf zone (see figures 4 *D*, 5 *D*, and 6 *D*). At this moment, we have no sound evidence to interpret this phenomenon.

The numerical model also significantly overestimates the turbulence intensity, which results in excessive energy dissipation, producing the lower wave crest as shown in figure 3 (*a*) and the excessive vertical mixing rate that causes the spreading of the

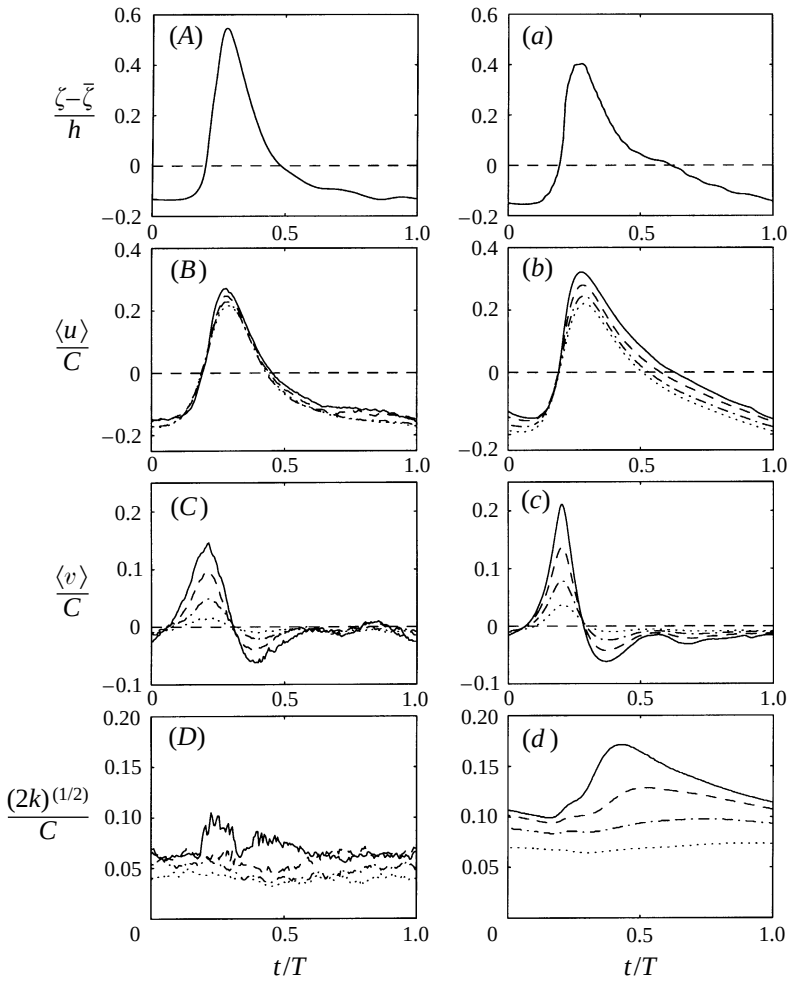

FIGURE 3. Comparisons of experimental data (*A–D*) and numerical results (*a–d*) at $(x-x_b)/h_b = 4.397; (y-\bar{\zeta})/h = -0.2623$ (—), -0.4909 (- - -), -0.7194 (- · - · -), -0.9080 (· · ·).

horizontal mean velocity across the water depth as shown in figure 3 (*b*). In fact, we have found from extensive numerical tests that the numerical model always overestimates the turbulence level near the breaking point. The primary reason is that the current turbulence closure model cannot accurately predict the initiation of turbulence in a rapidly distorted shear flow region such as the initial stage of wave breaking. The uncertainties in the initial and inflow boundary conditions for turbulent kinetic energy also introduce difficulties in accurately predicting the breaking point. In addition, due to the limitation of numerical resolution, the model cannot capture the details of the small overturning jet at the point of breaking, which is the major source of turbulence, and thus cannot handle accurately the turbulence generation during this time period. Fortunately, after the wave breaks and the resulting bore starts to propagate in the onshore direction, the small-scale effect of the overturning jet is no longer important. Therefore, the model can simulate both the turbulence field and mean flow field in the surf zone away from the breaking point very well.

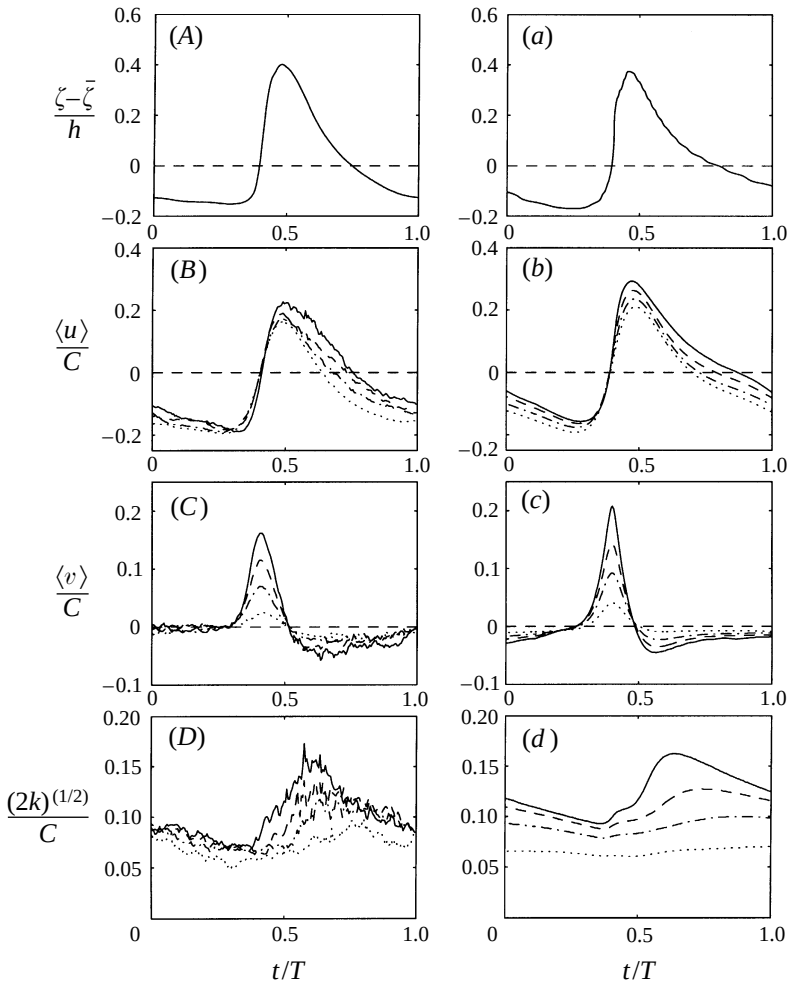

FIGURE 4. Comparisons of experimental data (*A–D*) and numerical results (*a–d*) at $(x-x_b)/h_b = 7.462; (y-\bar{\zeta})/h = -0.2957$ (—), -0.4820 (- - -), -0.6683 (- · - · -), -0.8857 (· · ·).

Figure 4 shows the comparisons at $(x-x_b)/h_b = 7.462$. The agreement between the numerical results and the measurements in terms of free-surface displacement and mean velocities is better than those shown in figure 3. These improvements are partially due to the better simulation of the turbulence field as shown in figure 4(*d*). Not only the turbulence pattern but also the turbulence intensity are accurately predicted by the numerical model. Both numerical and experimental results show that in the upper level, the turbulence intensity is highly correlated to the surface profile, while in the lower level the turbulence intensity remains almost constant during one wave cycle. In the following detailed analysis of the turbulence transport, we shall show that this difference is mainly caused by the different turbulence transport mechanisms at different elevations.

Figures 5 and 6 show the comparisons at the cross-sections $(x-x_b)/h_b = 10.528$ and $(x-x_b)/h_b = 13.618$, respectively. From these two figures, the wave heights are seen to decay in the onshore direction, indicating continuous energy dissipation of mean flow due to the turbulence energy extraction and dissipation. The overall agreement

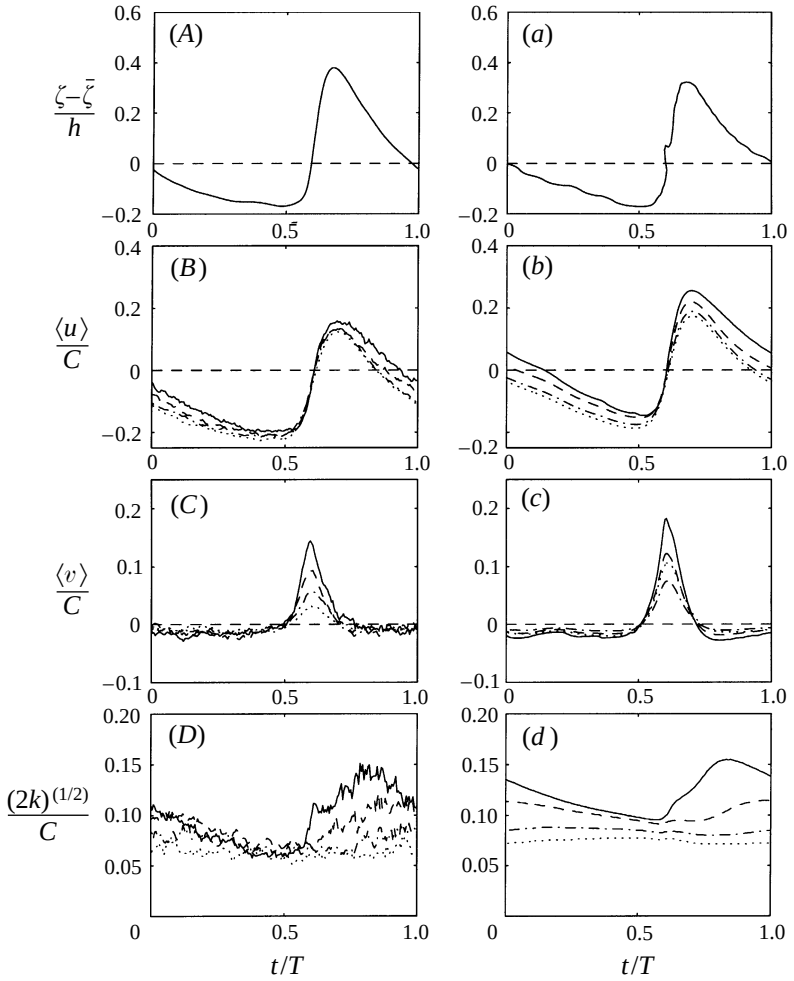

FIGURE 5. Comparisons of experimental data (*A–D*) and numerical results (*a–d*) at $(x - x_b)/h_b = 10.528; (y - \bar{\zeta})/h = -0.2736$ (—), -0.4764 (- - -), -0.6791 (- · - · -), -0.8142 (· · ·).

between the numerical results and the experimental measurements is fairly good for the mean free-surface displacement, mean velocities, and turbulence intensity.

From figures 4 to 6, the turbulence patterns are similar in the surf zone with intensity roughly proportional to C or $(gh)^{1/2}$. To show this similarity more clearly, we overlap the time histories of normalized turbulence intensity at the three vertical cross-sections (figure 7). Only the highest elevations, which have the strongest turbulence intensity, are shown. To exhibit the similarity, the normalized turbulence intensity curves are shifted by $0.2T$ for the section $(x - x_b)/h_b = 10.528$ and $0.4T$ for the section $(x - x_b)/h_b = 13.618$ (see figure 7). Although in the measurements, the highest elevations at different cross-sections were not exactly at the same normalized level, the similarity of the turbulence field in the surf zone is still evident. This feature is quite different from that in plunging breaking waves (Ting & Kirby 1995). In plunging breaking waves, the turbulence under the trough level gradually spreads out as the broken wave propagates and creates a quite different turbulence pattern at different locations in the surf zone. Therefore, it is possible to distinguish the breaker type not

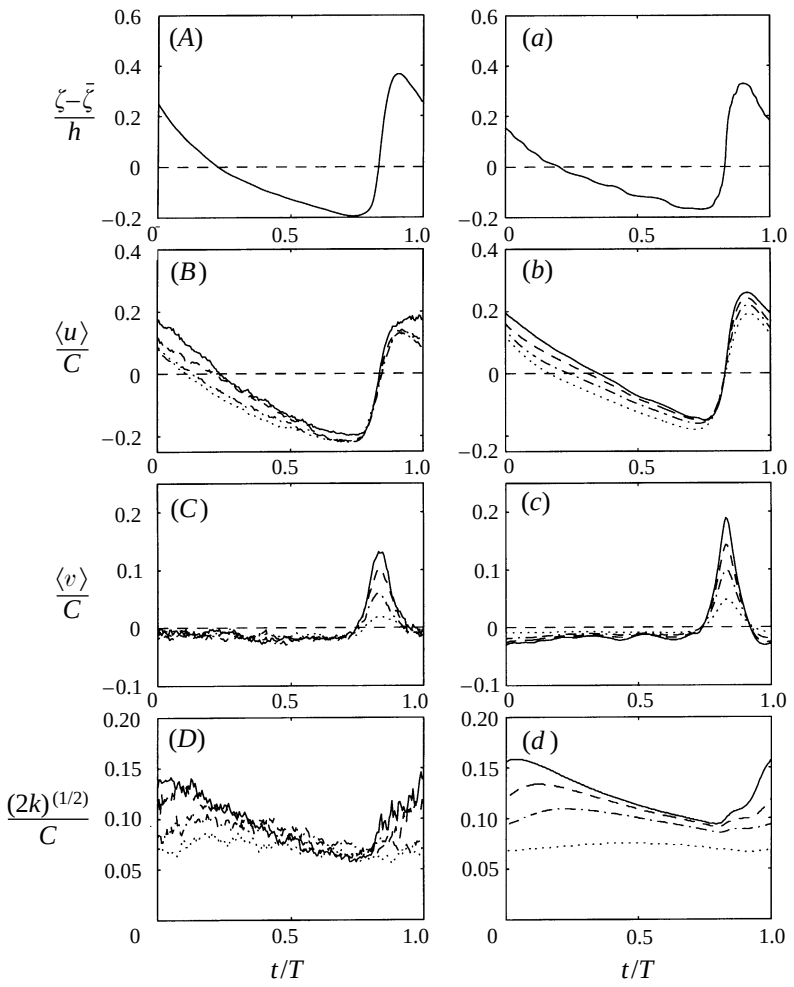

FIGURE 6. Comparisons of experimental data (*A–D*) and numerical results (*a–d*) at $(x - x_b)/h_b = 13.618; (y - \bar{\zeta})/h = -0.3226$ (—), -0.4729 (- - -), -0.6233 (- · - · -), -0.8489 (· · ·).

only by the shape of breaker tips but also by the resulting turbulence field under the broken wave.

The similarity of the turbulence field in the surf zone can also be manifested by investigating the time-average turbulence intensity, $V_T(y) = (1/T'(y)) \int_0^T [2k(t, y)]^{1/2} \mathrm{d}t$, in which $T'(y)$ refers to the effective time that the position y is occupied by water in one wave period. The vertical variations of $V_T(y)/C$ at different measurement sections from both numerical results and experimental data are shown in figure 8. The similarity of normalized V_T in the surf zone is clearly observed. In addition, the numerical results indicate that there exist two major regions of similarity of turbulence intensity, namely the turbulence production region which is above the trough level and has a rather large vertical gradient of turbulence intensity, and the lower region below the trough level which has relatively small vertical variations of turbulence intensity. Most measurements are limited to the lower region, in which the present model slightly overestimates the vertical gradient of turbulence intensity.

The similarity of the turbulence field also shows up in time-average eddy vis-

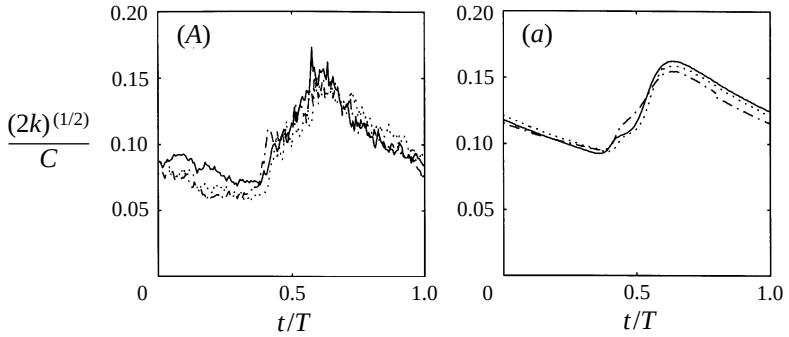

FIGURE 7. Experimental data (A) and numerical results (a) for normalized turbulence intensity at $(x - x_b)/h_b = 7.462$ and $(y - \bar{\zeta})/h = -0.2957$ (—), $(x - x_b)/h_b = 10.528$ and $(y - \bar{\zeta})/h = -0.2736$ (- · - ·), and $(x - x_b)/h_b = 13.618$ and $(y - \bar{\zeta})/h = -0.3226$ (· · ·). The curve - · - · has been shifted to the left by $t/T = 0.2$ and · · · by $t/T = 0.4$.

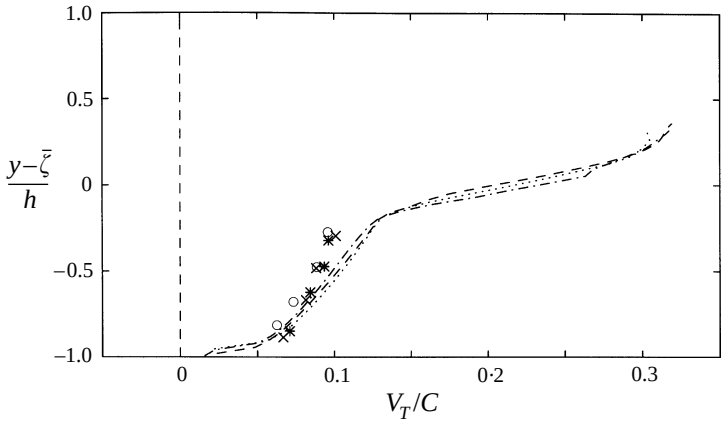

FIGURE 8. Computed (lines) and measured (symbols) time-average turbulence intensity $V_T(y) = (1/T'(y)) \int_0^T [2k(t, y)]^{1/2} dt$ at three measurement locations $(x - x_b)/h_b = 7.462$ (- - - and ×), $(x - x_b)/h_b = 10.528$ (- · - · and ○), $(x - x_b)/h_b = 13.618$ (· · · and ∗).

cosity, $v_T(y) = (1/T'(y)) \int_0^T v_t(t, y) dt$. Figure 9 gives the numerical results of the vertical variations of normalized $v_T(y)/(hC)$ at different measurement sections. The simulated $v_T/(hC)$ has a very similar pattern at different locations. The stratification for eddy viscosity is not as obvious as for turbulence intensity and the vertical distribution of $v_T(y)/(hC)$ can be approximated by a parabolic curve, $v_T(y)/(hC) = C_v\left((y + h - \bar{\zeta}/h)^{1/2}\right)^{1/2}$, where $C_v = 0.0077$. The maximum values of $v_T/(hC)$ are about 0.012 in this computation, which is of the same order of magnitude as the values suggested by Svendsen, Schäffer & Hansen (1987).

4.3. *Mean velocities and pressure field*

In this section, we use the numerical model to further explore some interesting physical mechanisms under the breaking wave which are difficult or even not feasible to investigate by laboratory experiments. First, we examine the time variations of the vertical distributions of mean velocities and pressure. Similar flow characteristics are observed at four locations. To be concise, in the following discussion, only the results at $(x - x_b)/h_b = 7.462$ are presented.

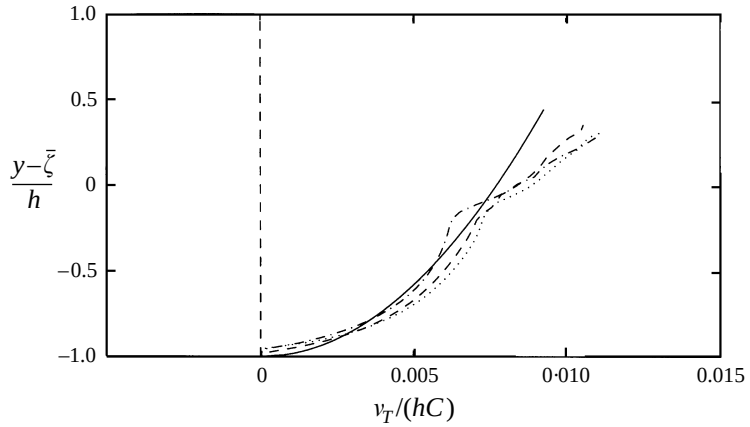

FIGURE 9. Computed time-average eddy viscosity $v_T(y) = (1/T'(y)) \int_0^T v_t(t, y)\mathrm{d}t$ at three measurement location: $(x - x_b)/h_b = 7.462$ (- - -), $(x - x_b)/h_b = 10.528$ (- · - ·), $(x - x_b)/h_b = 13.618$ (· · ·), and the fitted parabolic curve (—).

The 'roller' has been defined as the aerated area of recirculating flow in the front of the turbulent bore (Battjes 1988). In the 'roller' region, the horizontal fluid particle velocity is roughly equal to the local phase velocity C. This 'roller' concept has been adapted by Schäffer *et al.* (1993) in their numerical model to simulate the wave breaking process. In their model, the vertical variation of horizontal velocity was divided into two regions with the upper region representing the 'roller' propagating at the phase velocity. Although the 'roller' concept has been widely used to describe the turbulent bore front in the surf zone, detailed measurements of velocity profile in the 'roller' region have not been reported mainly because of the difficulties in obtaining accurate measurements in the aerated region.

Figure 10 provides the simulation results at the location of $(x - x_b)/h_b = 7.462$: figure 10(*a*) shows the time history of the free-surface elevation, and figure 10(*b*) displays the vertical variations of the normalized mean horizontal velocities, $\langle u \rangle / C$, at $t/T = 0.05, 0.25, 0.45, 0.65$, and 0.85. The 'roller' region exists in the upper level of the breaking wave front with the mean particle velocity about 80% of the local phase velocity C. In the lower part, beneath the trough level, the mean velocity field is little affected by the breaking process which leads to a rather uniform velocity distribution. From the numerical simulation, there exists a transition region within which the mean horizontal velocity decreases gradually from the 'roller' region to the lower part of the wave (figure 10*b*). The thickness of this transition region is about three times of that of the 'roller'. A similar phenomenon was observed in laboratories for turbulent bores by Peregrine & Svendsen (1978) and it served as the basis approximating the velocity distributions in surf zone (Svendsen & Madsen 1984). This transition region is very important for the turbulence transport processes which we shall discuss later.

The magnitude of the vertical velocity decreases linearly with the distance below the trough level (figure 10*c*). At the breaking wave front where the wave becomes steep, the maximum vertical velocity appears near the time-average water surface elevation and it decreases toward the crest of the wave. From figure 10(*b*) and figure 10(*c*), apart from in the region very close to the propagating turbulent bore, both horizontal and vertical velocities behave similarly to those in the non-breaking wave, i.e. the horizontal velocity is nearly uniform over the depth and the vertical velocity increases linearly from the bottom. This feature is observed at all other measurement sections

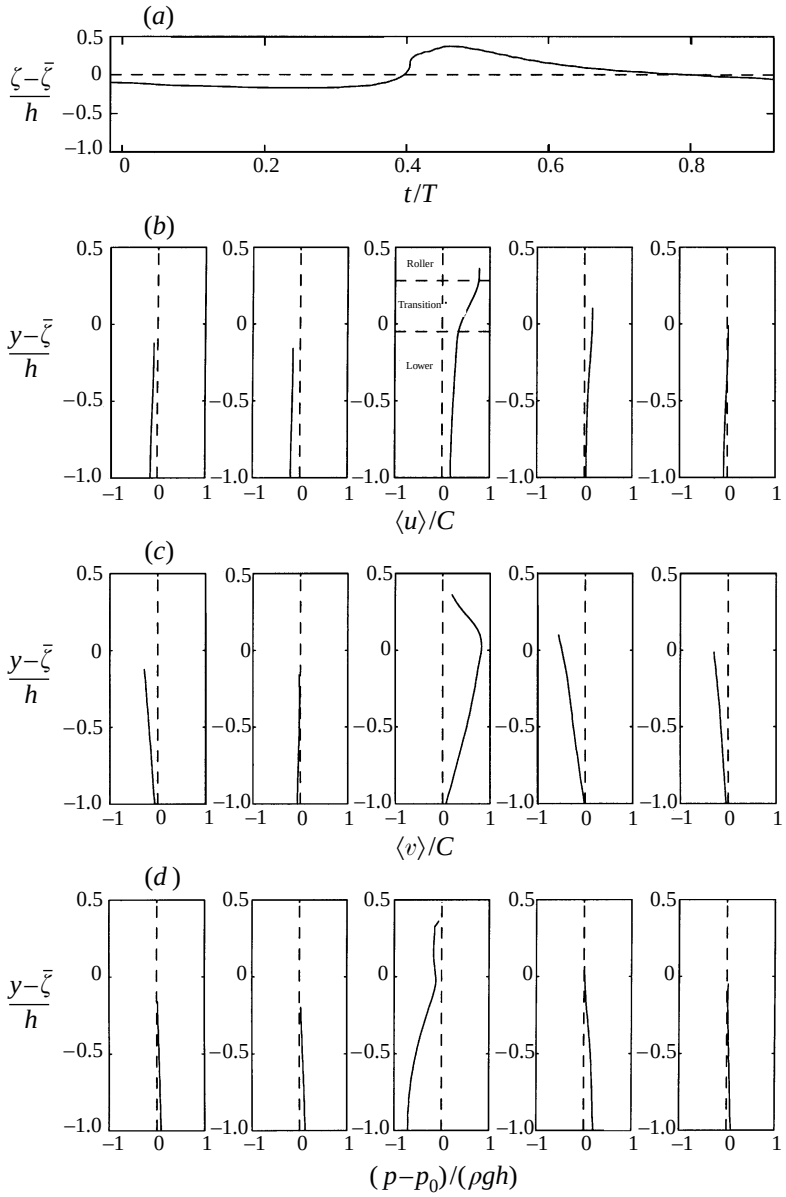

FIGURE 10. Computed free-surface profile (*a*), mean velocities (*b*, *c*), and pressure difference between actual pressure p and hydrostatic pressure p_0 (*d*) at $(x - x_b)/h_b = 7.462$ and $t/T = 0.05$, 0.25, 0.45, 0.65, and 0.85.

downstream of the breaking point, suggesting that the breaking process is a fairly local process and its direct influence on the rest of the wave motions through the turbulence field is not very significant. We shall discuss this in more detail in the next section.

It is well known that for non-breaking shallow-water waves, hydrostatic pressure is a good assumption. The assumption of hydrostatic pressure dramatically simplifies the derivation of depth-average equations, i.e. shallow-water equations, which can be applied to the very large-scale computations such as tsunami simulation (Liu *et al.*

1993). For breaking waves, due to the relatively strong vertical motion under the breaking wave front, it is generally not clear if the hydrostatic pressure assumption is still valid. The simulation results produced by our numerical model provide the opportunity to validate the hydrostatic pressure assumption. In figure 10 (*d*), the difference between the computed pressure and hydrostatic pressure is plotted. Under the wave trough, the mean pressure distribution is almost hydrostatic. Under the breaking wave front, due to the particle deceleration, the magnitude of the pressure is less than the hydrostatic pressure by about 7% near the bottom.

4.4. *Turbulence transport mechanisms*

From figures 7 to 9, the similarity of the turbulence field below the trough level in the surf zone is evident. However, since the laboratory measurements were only conducted below the trough level, information on the turbulence field and turbulence transport in the upper aerated region is missing. In this section, we attempt to fill in the missing information by using the numerical results. In the following discussion, each individual term in the turbulent kinetic energy transport equation (2.10) calculated from the numerical results is plotted as a function of time for selected elevations. By analysing the relative importance of each transport term, we should be able to determine the dominant turbulence transport mechanisms at a particular elevation. The analyses will be made in both the lower region, where the analyses can be validated against the measured turbulence data, and the upper region, where experimental data are not available. We again only show the analyses at $(x - x_b)/h_b = 7.462$.

We first examine the turbulence transport in the upper region, $(y - \bar{\zeta})/h = -0.0870$, as shown in figure 11 (*b*). This elevation is in the lower part of the transition region (see figure 10). With the passage of the turbulent bore front, there is a sharp increase of $\partial k/\partial t$, which indicates the rapid increase of turbulent kinetic energy. The major contribution to this large rate of change of turbulent kinetic energy is the turbulence production and vertical diffusion (figure 11 *b*). Since this elevation is in the transition region, it is not surprising that the turbulent kinetic energy is contributed by both the turbulence production induced by the relatively large velocity gradient and the downward turbulent diffusion from the 'roller' region where the turbulent kinetic energy is the strongest. We shall see this more clearly when we later plot the spatial distribution of turbulent kinetic energy. From figure 11 (*b*), we also see that the rate of k change drops very quickly after the passage of the bore front due to the reduction of turbulence production and diffusion. Another important mechanism is the vertical convection, $\langle v \rangle \partial k/\partial y$, which most of the time is positive and acts to reduce the turbulent kinetic energy. The positive $\langle v \rangle \partial k/\partial y$ is caused by the simultaneous positiveness of both $\langle v \rangle$ and $\partial k/\partial y$, which acts to transport the low-turbulence flow in from the lower part of wave.

The turbulence transport mechanisms about 3.4 cm lower are quite different (figure 11 *c*). This elevation corresponds to the highest one in the laboratory measurements (solid lines in figures 4 *D* and 4 *d*). All quantities are almost one order of magnitude smaller than those appearing in figure 11 (*b*). One outstanding feature of the turbulence transport at this elevation is the existence of two peaks in $\partial k/\partial t$. The first peak is mainly caused by the turbulence production mechanism which is closely correlated to the passage of the bore front. The vertical convection again plays the role of reducing the turbulent kinetic energy by advecting the low-turbulence flow in. But the vertical diffusion contributes little to the first peak. Instead, the time lag makes the peak of vertical diffusion occur about $0.1T$ later than the peak of turbulence production and thus contributes to the second, but higher, peak of the

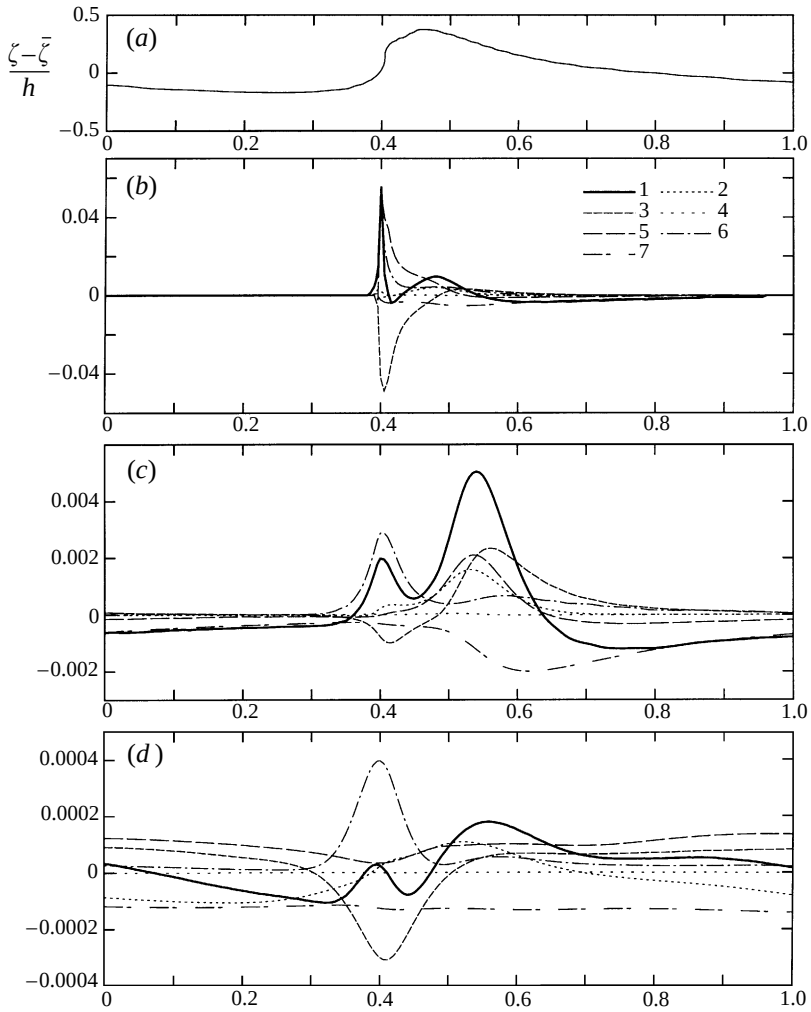

FIGURE 11. Computed free-surface profile (*a*); and transport terms for k in equation (2.10) at $(x_b - x)/h_b = 7.462$ and $(y - \bar{\zeta})/h = -0.0870$ (*b*), -0.2957 (*c*), and -0.8857 (*d*). All terms are normalized by $g(gh)^{1/2}$; 1: time rate of change of k, 2: negative horizontal convection $(-\langle u\rangle(\partial k/\partial x))$, 3: negative vertical convection $(-\langle v\rangle\partial k/\partial y)$, 4: horizontal diffusion, 5: vertical diffusion, 6: turbulent production, 7: turbulent dissipation.

rate of change of turbulent kinetic energy. In the meantime, the vertical convection changes to contribute to the increase of turbulence due to the change of the mean vertical velocity from positive to negative after the passage of the wave front (see figure 10). The horizontal convection also starts to contribute by bringing in the upstream flow with now higher turbulence intensity caused by the passage of the turbulent bore. Together with the gradually decreasing turbulence production mechanism, the convection and vertical diffusion overwhelm the increasing turbulence dissipation to create the second peak in the increase of turbulent kinetic energy. Under any circumstances, the horizontal diffusion is negligibly small compared with the rest of terms. About $0.2T$ after the wave front passes, the dissipation term gradually suppresses the rest of the turbulent contributions and the turbulent kinetic energy starts to decrease.

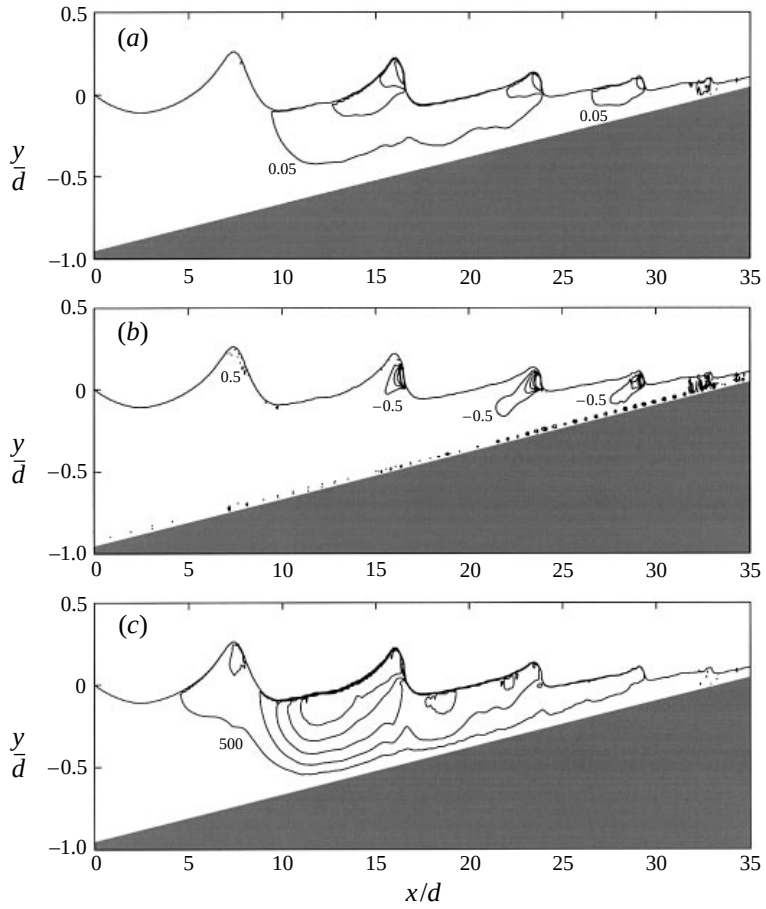

FIGURE 12. Computed normalized (*a*) turbulence intensity $(2k)^{1/2}/\,[g(d_c+a)]^{1/2}$ (0.05 to 0.20 with interval of 0.05), (*b*) mean vorticity $\omega/\left[g/(d_c+a)\right]^{1/2}$ [−0.5 to −2.5 with interval of −0.5 (—) and 0.5 (· · ·)], and (*c*) eddy viscosity ν_t/ν (500 to 2500 with interval of 500) at $t/T = 0.0$.

Moving about 9.5 cm downwards, which corresponds to the lowest elevation in the laboratory measurements (dotted line in figure 4*D* and 4*d*), one observes another transport mechanism. The turbulence production is again closely correlated to the passage of the bore front but of much smaller magnitude compared to those at the upper elevations. Overcoming the negative contribution by the vertical convection and the almost constant dissipation, the production creates a very small peak in the change rate of turbulent kinetic energy. After the passage of the turbulent bore, the total contribution of the turbulence energy increase is almost exactly balanced by the dissipation mechanism and thus results in the nearly equilibrium state of turbulence field.

4.5. *Spatial distribution of turbulent and vortical field*

Another advantage of the numerical model is its ability to display the mean vortical field and the turbulence field in the spatial domain. In this section, we show two snapshots at $t/T = 0$ and $t/T = 0.4$ of turbulence intensity, mean vorticity, and eddy viscosity (figure 12 and figure 13).

The normalized turbulence intensity is shown in figure 12 (*a*). The highest turbulence

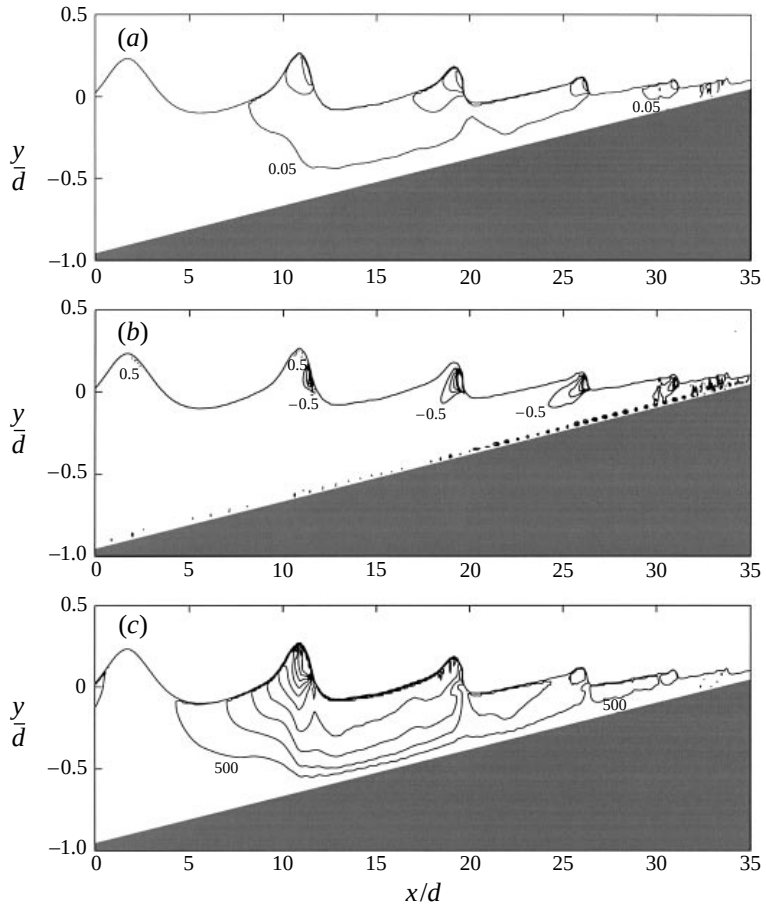

FIGURE 13. Computed normalized (*a*) turbulence intensity $(2k)^{1/2}/\left[g(d_c+a)\right]^{1/2}$ (0.05 to 0.20 with interval of 0.05), (*b*) mean vorticity $\omega/\left[g/(d_c+a)\right]^{1/2}$ [−0.5 to −2.5 with interval of −0.5 (—) and 0.5 (· · ·)], and (*c*) eddy viscosity ν_t/ν (500 to 5000 with interval of 500) at $t/T = 0.4$.

intensity appears in the 'roller' region. As the wave propagates forward, the turbulent kinetic energy gradually decreases but with very similar patterns of turbulence distribution accompanied by the decaying wave amplitude (figure 13 *a*). All these agree qualitatively with the experimental observation and theoretical expectation. However, as we have mentioned before, our numerical model predicts the initiation of turbulence earlier before the wave front reaches the measured breaking point. This becomes obvious from figure 13 (*a*) which shows the snapshot at $t/T = 0.4$. From this figure, we observe that turbulence starts to appear at $x/d_c = 10$ instead of at $x/d_c = 16$, the measured breaking point. It is one of our future tasks to resolve this problem.

It has been observed by many researchers that horizontal vortices are generated under the breaking wave (e.g. Nadaoka *et al.* 1989). However, direct computations for the mean vortical field under breaking waves are rare. Figures 12 (*b*) and 13 (*b*) show the normalized mean vortical field under the breaking wave. The vorticity is generated at the toe of the wave front and is then left behind by the wave and convected to the deeper region when the wave passes. The source of vorticity is generally in the transition region, while the source of turbulence is in the 'roller' region above

the transition region. The vorticity transport also exhibits a different feature from turbulence transport. It is mainly caused by the unique vorticity generation and destruction mechanisms under a breaking wave. In the breaking wave, the mean vorticity is created on the free surface and diffuses into the interior region. There are no significant production and destruction mechanisms in the interior region to change the total amount of vorticity and the diffusion and convection are the only two processes that redistribute the vorticity. The mean vorticity can only be destroyed on either the free surface or the bottom. From the numerical simulation, it is seen that the normalized vorticity under the turbulent bore is of the order of magnitude of $O(1)$ to $O(10)$ and it is negative (clockwise). The vorticity generated on the bottom is almost one order of magnitude smaller than that generated by the turbulent bore and it can be either positive or negative (not shown clearly in this plot), varying in both time and space.

It is noted that there is positive (counter-clockwise) vorticity predicted by the model in the crest region before the wave breaks, which is much smaller than the negative vorticity generated by the breaking wave. The existence of such small positive vorticity is caused by the enforcement of the zero shear stress on the free surface. According to Longuet-Higgins (1992), the vorticity on the free surface must be given by $\omega_s = -2\kappa q$, where κ is the curvature of the streamline and q is the tangential particle speed. Therefore, for non-breaking waves, the maximum surface vorticity ω_s always occurs at the crest where both the particle velocity and streamline curvature are maximum. However, the thickness of the surface vortical layer, which can be estimated by $l_s = (\nu T)^{1/2}$ for a periodic wave, is generally very small. Therefore, unlike the vorticity generated by the breaking wave, the positive surface vorticity has little impact on the interior flow field.

It is also noted that both turbulence intensity and mean vorticity are mainly concentrated in the regions very close to breaking wave fronts. In other regions, these two quantities are rather small, which suggests that the mean flow is almost a potential flow with little influence from the breaking processes. This supports our earlier statement that the spilling breaking is a rather local process with its effect mainly confined in the region close to the breaking front.

The eddy viscosity is another important parameter which measures the mixing rate for both momentum and substances. The spatial distribution of computed eddy viscosity is presented in figures 12 (*d*) and 13 (*d*). The eddy viscosity has been normalized by the molecular viscosity $\nu = 1.0 \times 10^{-6} \mathrm{m}^2\ \mathrm{s}^{-1}$. The eddy viscosity has a very different distribution from that of turbulence intensity. As the water depth decreases, the eddy viscosity decreases faster in the onshore direction than the turbulence intensity. This is mainly caused by the fact that the eddy viscosity is proportional to the turbulence length scale l and turbulence intensity $(2k)^{1/2}$, i.e., $\nu_t \sim l\, k^{1/2}$, both of which decrease as the water depth decreases. Therefore, compared with the turbulence intensity $(2k)^{1/2}$, eddy viscosity decreases much faster because of the simultaneous decrease of l which is generally proportional to the water depth in the surf zone.

5. Concluding remarks

In this paper, we have presented a numerical model which can be used to simulate breaking waves in the surf zone. By applying it to the spilling wave breaking problem, we found that the model results compare very well with experimental data, especially in the inner surf zone. The following wave or turbulence characteristics for the spilling

breaking wave in the surf zone are either confirmed or found by the numerical simulation.

(i) There exists a 'roller' region in the breaking wave front with a mean particle velocity of at least 80% of the local wave celerity. The 'roller' is a source region of turbulence generation. In the lower region below the trough level, the mean horizontal velocity is nearly uniform. In between, there exists a transition region with thickness about three times of that of the 'roller' region. The particle velocity in this region decreases gradually from the 'roller' region to the lower part of the wave. The mean vorticity is generated in the transition region.

(ii) The pressure distribution under the spilling breaking wave is almost hydrostatic. The maximum deviation from hydrostatic pressure is only 7%, which occurs under the broken wave front.

(iii) The spilling breaking process is a rather local phenomenon. Except in the region very close to the breaking wave front, both mean vorticity and turbulence intensity are very weak.

(iv) In the surf zone, there exists a similarity region for the turbulence field. In this region, the time histories of the turbulence intensity at different vertical cross-sections are similar with their magnitudes proportional to C. The vertical variations of the time-average turbulence intensity and eddy viscosity are also similar with their magnitudes proportional to C and hC, respectively.

(v) The turbulence transport mechanisms are quite different at different elevations in the surf zone. In the transition region between the 'roller' region and the bottom region, the dominant mechanisms are turbulence production, vertical diffusion, and vertical convection. The first two contribute to the increase of turbulence but the last reduces the turbulence. In the bottom region, all turbulence transport mechanisms become very weak (two orders of magnitude smaller than those in the transition region) and thus the turbulence level is nearly constant during one wave period. In between, all turbulence transport mechanisms are active except the horizontal diffusion. The production, which is correlated with the passage of the breaking wave front, is responsible for the first increase of the rate of change of turbulent kinetic energy. The convection and vertical diffusion are responsible for the second but larger increase of the rate of change of turbulent kinetic energy, which occurs about $0.1T$ after the passage of the wave front. The dissipation then gradually grows and finally overcomes all the turbulent contributions, causing a decrease of the rate of change of turbulent kinetic energy.

We have performed sensitivity analyses for the coefficients in the k–ϵ model. The only sensitive coefficient was $C_{1\epsilon}$, which controls the 'production' rate of turbulence dissipation. A 10% change of this coefficient from its suggested value would result in more than a 50% change of total turbulent kinetic energy in the surf zone after the wave breaks, which causes a significant change of wave profile. A 10% change of other coefficients from their suggested values, however, only cause less than a 10% change of total kinetic energy in the surf zone, which has little influence on the wave profile. In view of the fact that our numerical results compare well with the experimental data we conclude that the recommended values for these coefficients should be used. We have also attempted to demonstrate the advantage of the new turbulence closure model over the conventional eddy viscosity model. By simulating the same problem and comparing the numerical results to the available experimental data, we found that the new model has produced consistently better results in terms of mean free-surface displacement, mean velocities and turbulence intensity.

We wish to thank Dr Douglas B. Kothe at Los Alamos Laboratories for providing the source code of RIPPLE on which our mean flow model is based. We also wish to thank Drs Francis C. K. Ting and James T. Kirby for providing the experimental data. Comments from Drs Nobuhisa Kobayashi and Ib Svendsen were also helpful and acknowledged. The research was supported, in part, by research grants from the National Science Foundation (CTS-9302203) and the Army Research Office (DAAL03-92-G-0116).

REFERENCES

Battjes, J. A. 1975 Modeling of turbulence in the surf zone. *Proc. Symp. on Modeling Tech., San Francisco*, pp. 1050–1061. ASCE.

Battjes, J. A. 1988 Surf-zone dynamics. *Ann. Rev. Fluid Mech.* **20**, 257–293.

Brocchini, M., Drago, M. & Ivoenitti, L. 1992 The modeling of short waves in shallow water: Comparison of numerical model based on Boussinesq and Serre equations. *Proc. 23rd Intl Conf. Coastal Engng*, pp. 76–88. ASCE.

Brocchini, M. & Peregrine, D. H. 1996 Integral flow properties of the swash zone and averaging. *J. Fluid Mech.* **317**, 241–273.

Champagne, F. H., Harris, V. G. & Corrsin, S. 1970 Experiments on nearly homogeneous turbulent shear flow. *J. Fluid Mech.* **41**, 81–139.

Chang, K. A. & Liu, P. L-F. 1997 Measurement of breaking waves using particle image velocimetry. *Proc. 25th Intl Conf. Coastal Engng*, pp. 527–536. ASCE.

Chorin, A. J. 1968 Numerical solution of the Navier–Stokes equations. *Math. Comput.* **22**, 745–762.

Chorin, A. J. 1969 On the convergence of discrete approximations of the Navier–Stokes equations. *Math. Comput.* **232**, 341–353.

Deigaard, R., Fredsoe, J. & Hedegaard, I. B. 1986 Suspended sediment in the surf zone. *J. Waterway, Port, Coastal Ocean Engng* **112**, 115–129.

Hattori, M. & Aono, T. 1985 Experimental study on turbulence structure under spilling breakers. In *The Ocean Surface* (ed. Y. Toba & H. Mitsuyasu), pp. 419–424. Kluwer.

Hirt, C. W. & Nichols, B. D. 1981 Volume of fluid (VOF) method for dynamics of free boundaries. *J. Comput. Phys.* **39**, 201–225.

Inman, D. L., Tait, R. J. & Nordstrom, C. E. 1971 Mixing in the surf zone. *J. Geophys. Res.* **76**, 3493–3514.

Johns, B. 1978 The modeling of tidal flow in a channel using a turbulence energy closure scheme. *J. Phys. Oceanogr.* **8**, 1042–1049.

Johns, B. & Jefferson, R. J. 1980 The numerical modeling of surface wave propagation in the surf zone. *J. Phys. Oceanogr.* **10**, 1061–1069.

Karambas, Th. V. & Koutitas, C. 1992 A breaking wave propagation model based on the Boussinesq equations. *Coastal Engng* **18**, 1–19.

Kothe, D. B., Mjolsness, R. C. & Torrey, M. D. 1991 *RIPPLE: A computer program for incompressible flows with free surfaces.* Los Alamos National Laboratory, LA-12007-MS.

Launder, B. E., Morse, A., Rodi, W. & Spalding, D. B. 1972 Prediction of free shear flows: a comparison of the performance of six turbulence models. *Free Shear Flow, NASA Conf.*, pp. 361–426.

Launder, B. E., Reece, G. T. & Rodi, W. 1975 Progress in development of a Reynolds stress turbulence closure. *J. Fluid Mech.* **68**, 537–566.

Launder, B. E. & Spalding, D. B. 1972 *Mathematical Models of Turbulence.* Academic.

Lemos, C. M. 1992 *Wave Breaking.* Springer.

Lin, J.-C. & Rockwell, D. 1994 Instantaneous structure of a breaking wave. *Phys. Fluids* **6**, 2877–2879.

Lin, J.-C. & Rockwell, D. 1995 Evolution of a quasi-steady breaking wave. *J. Fluid Mech.* **302**, 29–44.

Liu, P. L.-F. & Lin, P. 1997 A numerical model for breaking wave: the volume of fluid method. *Research Rep.* CACR-97-02. Center for Applied Coastal Research, Ocean Eng. Lab., Univ. of Delaware, Newark, Delaware 19716.

Liu, L.-F. P., Yoon, S. B., Seo, S. N. & Cho, Y. 1993 Numerical simulation of tsunami inundation at Hilo, Hawaii. *Tsunami '93, Proc. IUGG/IOC Intl Tsunami Symp., Wakayama, Japan.*

Longuet-Higgins, M. S. 1992 Capillary rollers and bores. *J. Fluid Mech.* **240**, 659–679.

Mizuguchi, M. 1986 Experimental study on kinematics and dynamics of wave breaking. *Proc. 20th Intl Conf. of Coastal Engng*, pp. 589–603. ASCE.

Nadaoka, K., Hino, M. & Koyano, Y. 1989 Structure of the turbulent flow field under breaking waves in the surf zone. *J. Fluid Mech.* **204**, 359–387.

Nadaoka, K. & Kondoh, T. 1982 Laboratory measurements of velocity field structure in the surf zone by LDV. *Coastal Engng in Japan* **25**, 125–146.

Peregrine, D. H. 1983 Breaking waves on beaches. *Ann. Rev. Fluid Mech.* **15**, 149–178.

Peregrine, D. H. & Svendsen, I. A. 1978 Spilling breakers, bores and hydraulic jumps. *Proc. 16th Coastal Engng Conf., Hamburg*, vol. 1, pp. 540–550. ASCE.

Rodi, W. 1980 *Turbulence Models and Their Application in Hydraulics – A State-of-the-Art Review*. IAHR Publication.

Schäffer, H. A. Madsen, P. A. & Deigaard, R. 1993 A Boussinesq model for waves breaking in shallow water. *Coastal Engng* **20**, 185–202.

Shih, T.-H., Zhu, J. & Lumley, J. L. 1996 Calculation of wall-bounded complex flows and free shear flows. *Intl J. Numer. Meth. Fluids* **23**, 1133–1144.

Skyner, D. 1996 A comparison of numerical predictions and experimental measurements of the internal kinematics of a deep water plunging wave. *J. Fluid Mech.* **315**, 51–64.

Stive, M. J. F. 1980 Velocity and pressure field of spilling breaker. *Proc. 17th Conf. Coastal Engng*, pp. 547–566. ASCE.

Stive, M. J. F. & Wind, H. G. 1982 A study of radiation stress and set-up in the nearshore region. *Coastal Engng* **6**, 1–25.

Svendsen, I. A. 1987 Analysis of surf zone turbulence. *J. Geophys. Res.* **92**, 5115–5124.

Svendsen, I. A. & Madsen, P. A. 1984 A turbulent bore on a beach. *J. Fluid Mech.* **148**, 73–96.

Svendsen, I. A. & Putrevu, V. 1994 Nearshore mixing and dispersion. *Proc. R. Soc. Lond.* A **445**, 561–576.

Svendsen, I. A. & Putrevu, V. 1996 Surf-zone hydrodynamics. In *Adv. Coastal Ocean Engng* **2**, 1–78.

Svendsen, I. A., Schäffer, H. A. & Hansen, J. B. 1987 The interaction between the undertow and boundary layer flow on a beach. *J. Geophys. Res.* **92**, 11,845–11,856.

Ting, F. C. K. & Kirby, J. T. 1994 Observation of undertow and turbulence in a laboratory surf zone. *Coastal Engng* **24**, 51–80.

Ting, F. C. K. & Kirby, J. T. 1995 Dynamics of surf-zone turbulence in a strong plunging breaker. *Coastal Engng* **24**, 177–204.

Ting, F. C. K. & Kirby, J. T. 1996 Dynamics of surf-zone turbulence in a spilling breaker. *Coastal Engng* **27**, 131–160.

Zelt, J. A. 1991 The run-up of nonbreaking and breaking solitary waves. *Coastal Engng* **15**, 205–246.